Promoting electrochemical ammonia synthesis by synergized performances of Mo_2C-Mo_2N heterostructure

Tae-Yong An[1†], Subramani Surendran[1†], Sebastian Cyril Jesudass[2], Hyunjung Lee[1], Dae Jun Moon[1], Jung Kyu Kim[3*] and Uk Sim[1,4,5*]

[1]Hydrogen Energy Technology Laboratory, Korea Institute of Energy Technology (KENTECH), Naju, Republic of Korea, [2]Department of Science and Engineering, Chonnam National University, Gwangju, Republic of Korea, [3]School of Chemical Engineering, Sungkyunkwan University, Suwon, Republic of Korea, [4]Research Institute, NEEL Sciences, INC, Jeollanamdo, Republic of Korea, [5]Center for Energy Storage System, Chonnam National University, Gwangju, Republic of Korea

Hydrogen has become an indispensable aspect of sustainable energy resources due to depleting fossil fuels and increasing pollution. Since hydrogen storage and transport is a major hindrance to expanding its applicability, green ammonia produced by electrochemical method is sourced as an efficient hydrogen carrier. Several heterostructured electrocatalysts are designed to achieve significantly higher electrocatalytic nitrogen reduction (NRR) activity for electrochemical ammonia production. In this study, we controlled the nitrogen reduction performances of Mo_2C-Mo_2N heterostructure electrocatalyst prepared by a simple one pot synthesis method. The prepared Mo_2C-$Mo_2N_{0.92}$ heterostructure nanocomposites show clear phase formation for Mo_2C and $Mo_2N_{0.92}$, respectively. The prepared Mo_2C-$Mo_2N_{0.92}$ electrocatalysts deliver a maximum ammonia yield of about 9.6 µg h^{-1} cm^{-2} and a Faradaic efficiency (FE) of about 10.15%. The study reveals the improved nitrogen reduction performances of Mo_2C-$Mo_2N_{0.92}$ electrocatalysts due to the combined activity of the Mo_2C and $Mo_2N_{0.92}$ phases. In addition, the ammonia production from Mo_2C-$Mo_2N_{0.92}$ electrocatalysts is intended by the associative nitrogen reduction mechanism on Mo_2C phase and by Mars-van-Krevelen mechanism on $Mo_2N_{0.92}$ phase, respectively. This study suggests the importance of precisely tuning the electrocatalyst by heterostructure strategy to substantially achieve higher nitrogen reduction electrocatalytic activity.

KEYWORDS

ammonia electrosynthesis, electrocatalyst, electrochemical nitrogen reduction reaction, heterostructures, Mo_2C catalyst, Mo_2N catalyst

1 Introduction

The modern technical society holds a shear desire for cost-effective, eco-friendly, and reliable energy technologies to mitigate pollution and ensure energy sustainability (Fiksel et al., 2014). Researchers and technologists have conceded with the development of hydrogen energy which was abundantly available and displayed potential applications in various sectors (Yue et al., 2021). However, the storage and transport of valuable fuel became an exceptional threat which involved complex storage facilities and cryogenic systems (Zhou et al., 2005). Ammonia was then ascertained as the effective hydrogen carrier, which can hold up to 17.65% of its total mass (Avery et al., 1988; MacFarlane et al., 2020). Ammonia can be transported over long distances under ambient conditions and could also be utilized as fuels directly (Zhao et al.,

2019). Nevertheless, ammonia is produced by the high energy-consuming Haber-Bosch (HB) process, which involves nitrogen and natural gas (CH_4), resulting in greenhouse gas (GHG) evolution (Kandemir et al., 2013; Safari et al., 2019). Technologies for eco-friendly and sustainable ammonia production are yearned to achieve supremacy over green energy.

Electrochemical nitrogen reduction reaction (NRR) is the most viable and simple technology developed for ammonia production. NRR involves water, N_2, and renewable electricity to generate ammonia over six proton-coupled electron transfer (PCET) steps (MacFarlane et al., 2020). NRR is facilitated over an electrocatalyst which must exhibit better activity, selectivity, and stability over NRR electrolysis (Cui et al., 2018). Since the triple bond of dinitrogen (N≡N) has a high dissociation energy of nearly 941 kJ mol^{-1}, NRR requires large overpotentials, which are much lower than required for hydrogen evolution reaction (HER) (Ren et al., 2021). Hence, HER becomes an active competitor for NRR, resulting in a lower ammonia yield rate and Faradaic efficiency (FE). Various electrocatalyst designs were engineered to increase activity for NRR and selectivity towards ammonia without the intermediate formation and HER (Du et al., 2021).

Mo-based electrocatalysts have been analyzed as the effective NRR electrocatalyst due to their higher affinity for nitrogen, as observed from the nitrogenase enzymes with Fe-Mo cofactors (Liu et al., 2020; Arif et al., 2023). The nitrogenase enzymes exhibit dominant HER, which makes them unfavorable for efficient ammonia production (Hinnemann and Nørskov, 2006). Several strategies were followed to design Mo-based electrocatalysts to achieve effective NRR performances (Guo et al., 2021). As an important design strategy, MoS_2 was synthesized as an NRR electrocatalyst which exhibits a sufficient ammonia yield but poor FE due to dominant HER (Zhang et al., 2018a). Therefore, Mo-based electrocatalysts must be engineered to achieve a higher ammonia yield and effectively suppress HER. In this way, Yesudoss et al. (Yesudoss et al., 2021) synthesized the γ-Mo_2N supported on h-BN sheets as an effective NRR electrocatalyst. γ-Mo_2N/BN hybrids, with strong interactions and bridging bonds between Mo_2N and BN, exhibit a superior NRR performance. Therefore, precise tuning of the electrocatalyst design can enhance the NRR activity with a high ammonia yield rate and FE.

Typically, Mo_2C electrocatalyst exhibits a Pt-like behavior, metallic nature, and better stability (Huo et al., 2016; Su et al., 2019). Thereby, Mo_2C nanodots embedded in carbon nanosheets (Mo_2C/C) were analyzed as an electrocatalyst for NRR, which initially revealed better ammonia yield even under strong hydrogen spillover (Cheng et al., 2018). This is attributed to the higher density of active sites in the Mo_2C/C electrocatalyst, which exhibited a low FE due to higher selectivity for HER. Henceforth, these electrocatalysts are engineered with Mo single-atom catalysts (MoSAs-Mo_2C) (Ma et al., 2020), MoO_2 quantum dots (Mo_2C-MoO_2) (Wan et al., 2022), and as Mo_2C nanorods (Ren et al., 2019), which reveal significantly high NRR performances. Notably, MoS_2/Mo_2C heterostructures were designed recently, which exhibited a high NRR FE of about 42% due to the selectivity of the Mo atoms towards N_2 adsorption (Ye et al., 2023). However, a low ammonia yield rate of nearly 1.41 µg h^{-1} cm^{-2} was observed. Besides, Mo_2N was identified as an effective electrocatalyst due to its high conductivity and ample active sites for redox reactions (Hargreaves, 2013; Mtukula et al., 2017). Therefore, Mo_2N was studied as an NRR electrocatalyst, which exhibited a high ammonia yield five times more than the prepared MoO_2 electrocatalyst indicating the

supreme activity of the N atoms in Mo lattice (Ren et al., 2018). Besides, Mo_2N electrocatalyst exhibited significant selectivity towards ammonia indicating the reliability of the Mo_2N electrocatalyst (Ren et al., 2018; Yesudoss et al., 2021). Even though, the Mo_2C and Mo_2N electrocatalysts exhibit considerable electrocatalytic NRR performances, the electrocatalysts actively performs HER resulting in decreased NRR efficiency. Therefore, the electrocatalysts must be engineered carefully to achieve higher NRR activity.

Consequently, tailoring the electrocatalysts through a heterostructure strategy can be adopted, which increases the electrocatalytic activity by synergizing the performances of two different structures (Su et al., 2019; Wan et al., 2022). Heterostructures provide structural and electronic modifications in the electrocatalysts by which tunable performances are achieved, which proliferate the electrocatalytic performances (Yuan et al., 2022). For instance, Chen et al. (Chen et al., 2022) modified the MoS_2 electrocatalyst with *in situ* generated MoO_2 and ZnO (MMZ) as heterostructures, revealing significantly better NRR performances. The MMZ electrocatalyst exhibited a five-fold increase in ammonia yield and FE compared to pristine MoS_2, which indicates the multiplied electrocatalytic activity of the MMZ heterostructures. Therefore, the heterostructure formation has been a promising strategy in tailoring the performances of the pristine moieties to achieve considerably higher NRR performances. Besides, Co_3O_4-Mo_2N heterostructures have revealed a high electrocatalytic activity due to the interfacial electronic effects between the two structures (Wang et al., 2022). The differential electron density between Mo_2N and Co_3O_4 phases has improved the electrocatalytic activity of the heterostructures. Several other reports have suggested improved electrocatalytic activity by choice of suitable nitride heterostructures as an efficient strategy for NRR electrocatalysts (Yesudoss et al., 2021; Chu et al., 2022). Hence, the Mo-based electrocatalysts can be tailored with appropriate elements to achieve significantly higher ammonia yield rate and efficiency.

The above studies have motivated the fabrication of the single-phase transition metal carbides and nitrides into a heterostructure as an effective NRR electrocatalyst. In the present work, we demonstrate the preparation of the Mo_2C-$Mo_2N_{0.92}$ nanocomposites and the analysis of NRR performances of the prepared electrocatalysts. Mo_2C-$Mo_2N_{0.92}$ nanocomposites reveal the heterostructure formation of Mo_2C and Mo_2N structures. The prepared Mo_2C-$Mo_2N_{0.92}$ electrocatalyst achieves a high ammonia yield rate of about 9.6 µg h^{-1} cm^{-2} and FE of nearly 10.15%, respectively. The enhanced NRR performances can be ascribed due to the synergistic activity of the heterostructures of Mo_2C and $Mo_2N_{0.92}$, respectively. Hence, this study suggests promising electrocatalytic performances of the heterostructured electrocatalyst by tuning the structural and electronic properties of the single moieties.

2 Experimental methods

2.1 Synthesis procedure of Mo$_2$C-Mo$_2$N

Typically, a stoichiometric ratio of the precursors, molybdenum chloride ($MoCl_5$) and urea ($CO(NH_2)_2$) were mixed together with 10 ml ethanol and aged on a hot plate at 80°C for 2–3 h. The as-prepared samples were further pyrolyzed at 800°C for 3 h under N_2 flow. Further, the samples were prepared by varying the urea-metal ratio to 2:1 and 3:1, termed Mo_2C-$Mo_2N_{0.92}$ and $Mo_2N_{0.92}$-Mo_2C, respectively.

2.2 Characterizations

The crystal structure and phase formation of the samples were examined by powder X-ray diffraction (XRD; Rint 1000, Rigaku, Japan) with Cu Kα radiation (λ = 1.5418 Å). X-ray photoelectron spectroscopy (XPS; K-ALPHA+, Thermo Scientific) was used to determine the oxidation states of the elements in the electrocatalyst. The morphology and microstructure of the electrocatalyst was investigated by scanning electron microscopy (SEM; JSM-7500F, JEOL, Japan) and transmission electron microscopy (TEM; JEM-2100F, JEOL, Japan), respectively.

The slurry prepared using PVDF, carbon black and prepared electrocatalysts in the ratio 1:1:8 was loaded on carbon cloth ($1 \times 1\,cm^2$) and dried in vacuum oven for further electrochemical studies. The electrochemical NRR studies were carried out in a three-electrode cell configuration using the VMP3-Biologic multi-channel potentiostat under 0.1 M KOH electrolyte with and without N_2 purging. Graphite rod and Hg/HgO were used as the counter and reference electrodes, respectively. The Hg/HgO potential ($E_{(Hg/HgO)}$) was converted into reversible hydrogen electrode (RHE) potential (E_{RHE}) using Equation 1.

$$E_{RHE} = E_{(Hg/HgO)} + 0.118\,V + 0.0591 \times pH \tag{1}$$

2.3 Quantitative evaluation of NRR

The ammonia content in the electrolyte after the chronoamperometry (CA) tests for 2 h at various applied potentials were measured using the colorimetric method. 5 ml of the collected electrolyte after CA tests was sampled with colouring agents and catalysts using the standard ammonia test kits. Then the intensity of the coloured solution was measured using the UV-vis spectrophotometer. The intensity of the respective UV curves at 680 nm were compared to the standard calibration graphs of ammonia to estimate the concentration of ammonia present in the solution. The calibration graphs were derived from UV curves prepared by various known concentration of standard NH_4Cl salt. The linear curves from the UV plots yield the calibration graphs for ammonia. Hence, the concentration of ammonia can be estimated from the UV curves for samples after CA tests and calibration graphs (Liu et al., 2020).

The ammonia yield rate and Faradaic efficiency (FE) of the prepared electrocatalysts can be estimated using Equation 2 and Equation 3, respectively (Liu et al., 2020).

$$Yield\,rate\,(\mu g\,h^{-1}cm^{-2}) = \frac{[NH_3]\left(\frac{\mu g}{ml}\right) \times V\,(ml)}{t\,(h) \times A\,(cm^{-2})} \tag{2}$$

$$FE\,(\%) = \frac{3 \times Yield\,(\mu g\,h^{-1}cm^{-2}) \times F\,(C\,mol^{-1})}{17.03\left(\frac{g}{mol}\right) \times j\,(mA\,cm^{-2})} \tag{3}$$

where, $[NH_3]$ represent the concentration (μg/ml) of the ammonia present in the corresponding electrolyte, V is the volume of the electrolyte (ml), t is the time of electrolysis (hours), A is the area of the electrode (cm^{-2}), F is the Faradaic constant (96485 C mol^{-1}), and j is the current density at CA tests (mA cm^{-2}), respectively.

3 Results and discussion

3.1 Structural and morphological analysis

Mo_2C-$Mo_2N_{0.92}$ is synthesized by the simple urea glass route (Figure 1A). Initially, the $MoCl_5$ precursors are mixed with alcohols which primarily forms Mo-ethoxide ($Mo(OC_2H_5)_5$) and the Cl$^-$ ions are released as HCl (Giordano et al., 2008). Further, mixing urea ($CO(NH_2)_2$) with the above solution replaces the ethoxide groups in $Mo(OC_2H_5)_5$ due to the high solubility of urea under the presence of metal ions (Equation 4). Urea is used as both C and N precursors for the formation of Mo_2C and Mo_2N, respectively. The C=O bond cleavage in urea replaces the ethoxide molecule in $Mo(OC_2H_5)_5$, and the urea moiety coordinates with the Mo^{5+} atom forming metal-urea complexes, Mo-$(OCN_2H_4)_5$ (Equation 5). (Sardar et al., 2005) After heat treatment, the metal-urea complex is reduced into the desired Mo_2N-Mo_2C nanocomposites (Equation 6). By varying the urea-to-metal ratio (R), dominant phases of Mo_2N and Mo_2C can be achieved, respectively. Thereby, a lower urea content in the urea-metal ratio results in the dominant phases of Mo_2C, and high urea content favors Mo_2N formation respectively.

The proposed reaction mechanisms are elucidated as follows.

$$MoCl_5 + C_2H_5OH \rightarrow Mo(OC_2H_5)_5 + HCl \tag{4}$$

$$Mo(OC_2H_5)_5 + CO(NH_2)_2 \rightarrow Mo-(OCN_2H_4)_5 \tag{5}$$

$$Mo^{5+} + R\,OCN_2H_4 \rightarrow Mo_2C-Mo_2N + NH_3 + HCN + CO_2 \tag{6}$$
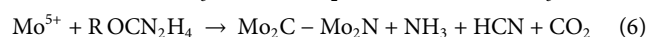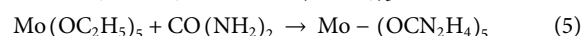
The structural analysis of the prepared samples was evaluated by X-ray diffraction (XRD) analysis. XRD patterns obtained for Mo_2C-$Mo_2N_{0.92}$ and $Mo_2N_{0.92}$-Mo_2C display crystalline peaks for the prepared samples (Figure 1B). The obtained peaks are well-matched to the respective phases of Mo_2C (JCPDS: 98–007–7158) and $Mo_2N_{0.92}$ (JCPDS: 98–015–8843). Similarly, XRD patterns for the bare Mo_2C samples reveal the respective well-matched phases. The simultaneous existence of the XRD patterns of the two phases without any peak shift or peak broadening can ascribe to the heterostructure formation. XRD patterns for Mo_2C-$Mo_2N_{0.92}$ prepared with 2:1 ratio reveals the dominant phases of Mo_2C with relatively smaller presence of $Mo_2N_{0.92}$ phases. Similarly, XRD patterns for $Mo_2N_{0.92}$-Mo_2C prepared with 3:1 urea to metal ratio displays the presence of dominant $Mo_2N_{0.92}$ phases with feeble Mo_2C phases, respectively. Thereby, a low urea content favors Mo_2C formation and a high urea content forms $Mo_2N_{0.92}$, respectively. Hence, $Mo_2N_{0.92}$ and Mo_2C phases exist together in a single system exhibiting differences in relative intensity of the XRD patterns without any peak shift or peak broadening. The relative intensity of the XRD patterns for the samples prepared at different urea to metal ratio explain the dominant phases of the Mo_2C and $Mo_2N_{0.92}$ moieties in the prepared electrocatalysts. Thus, the urea-metal ratio is the phase-determining factor for Mo_2N and Mo_2C.

The chemical states of the prepared Mo_2C-$Mo_2N_{0.92}$ and $Mo_2N_{0.92}$-Mo_2C samples were evaluated by the X-ray photoelectron spectroscopy (XPS) analysis. The Mo 3d spectra in Figure 1C can be deconvoluted into two peaks at 232.8 eV and 236 eV for Mo 3d$_{5/2}$ and Mo 3d$_{3/2}$, respectively. The small peak arising at the lower binding energy around 228.8 eV corresponds to the metallic Mo species for both Mo_2C-$Mo_2N_{0.92}$ and $Mo_2N_{0.92}$-Mo_2C samples. The C 1s spectra in Figure 1D display three deconvoluted peaks at 284.6 eV, 286.8 eV, and 289 eV corresponding to the sp-carbon (C=C) bonds (Yue et al.,

FIGURE 1
(A) Schematic representation of the synthesis procedure for Mo$_2$C-Mo$_2$N nanocomposites. **(B)** XRD patterns for the prepared Mo$_2$C-Mo$_2$N$_{0.92}$, Mo$_2$N$_{0.92}$-Mo$_2$C and bare Mo$_2$C samples, respectively. XPS spectra of **(C)** Mo 3d, **(D)** C 1s, and **(E)** N 1s for the prepared Mo$_2$C-Mo$_2$N$_{0.92}$ and Mo$_2$N$_{0.92}$-Mo$_2$C samples.
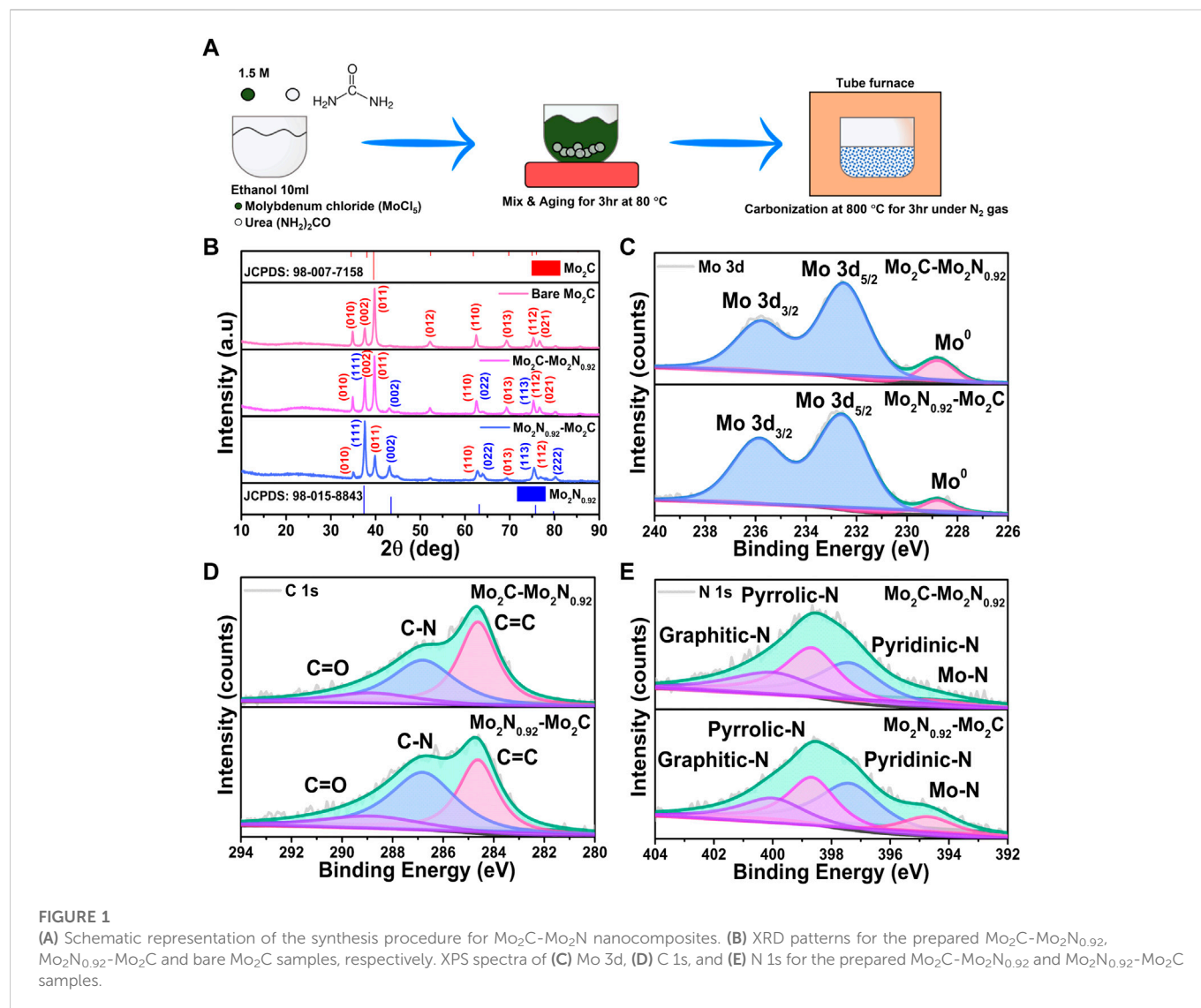
2021), N doped carbon (C-N), and feeble C=O signals due to incomplete decomposition of urea (CO(NH$_2$)$_2$), respectively. The deconvoluted N 1s spectra in Figure 1E display major peaks at 397.4 eV, 398.7 eV, and 400 eV, corresponding to pyridinic-N, pyrrolic-N, and graphitic-N, respectively. Besides, the feeble peak around 394.8 eV suggests the presence of Mo-N bonds in the prepared samples (Zhang et al., 2022). Evidently, the Mo$_2$N$_{0.95}$-Mo$_2$C samples reveal relatively higher intensity for Mo-N bonds compared to Mo$_2$C-Mo$_2$N$_{0.92}$, which validates the dominant presence of Mo$_2$N$_{0.92}$ in the prepared sample.

The morphological and microstructure studies were observed using scanning electron microscopy (SEM) and high-resolution transmission electron microscopy (HRTEM) analyses. SEM images for the prepared Mo$_2$C-Mo$_2$N$_{0.92}$ samples reveal the uniform distributions of the nanocomposites anchored to a substrate. SEM images of Mo$_2$C-Mo$_2$N$_{0.92}$ sample reveal the average sizes of the nanocomposites around ~50 nm (Figure 2A). HRTEM analysis reveals the lattice spacing of about 0.26 nm for Mo$_2$C-Mo$_2$N$_{0.92}$ nanocomposites corresponding to (010) lattice planes of Mo$_2$C (Figure 2B). The inset of Figure 2B shows the FFT patterns for the

Mo$_2$C-Mo$_2$N$_{0.92}$ sample, which reveal the crystalline phases of Mo$_2$C. Similarly, the SEM images in Figure 2C reveal the average sizes of the nanocomposites around ~110 nm for Mo$_2$N$_{0.92}$-Mo$_2$C. The HRTEM analysis for Mo$_2$N$_{0.92}$-Mo$_2$C sample reveals the lattice spacing of about 0.23 nm corresponding to (101) lattice planes of Mo$_2$C (Figure 2D). Furthermore, the intensity-line profiles for Mo$_2$C-Mo$_2$N$_{0.92}$ and Mo$_2$N$_{0.92}$-Mo$_2$C samples, as shown in the inset of Figures 2B, D, display an average interplanar distance of nearly 0.26 nm for Mo$_2$C-Mo$_2$N$_{0.92}$ and 0.23 nm for Mo$_2$N$_{0.92}$-Mo$_2$C, respectively.

3.2 Electrochemical NRR performance

Electrochemical NRR performances of the prepared electrocatalysts were performed under constant N$_2$ purging. Linear sweep voltammetry (LSV) performed under Ar- and N$_2$-saturated electrolyte reveals a lower onset with higher current density under N$_2$ saturation for Mo$_2$C-Mo$_2$N$_{0.92}$ electrocatalyst due to the occurrence of NRR (Figure 3A). NRR performances were quantified by the chronoamperometric (CA) measurements
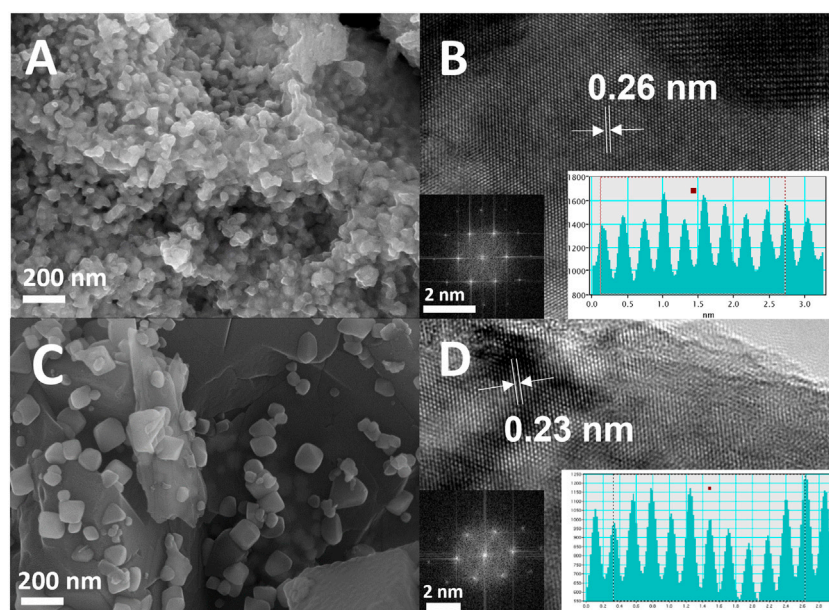
FIGURE 2
(A) SEM image, **(B)** HRTEM image (inset: FFT analysis and intensity-line profile) for Mo_2C-$Mo_2N_{0.92}$ sample, **(C)** SEM image, **(D)** HRTEM image (inset: FFT analysis and intensity-line profile) for $Mo_2N_{0.92}$-Mo_2C sample.

performed for 2 h under N_2-saturation at various applied potentials. The electrolytes were sampled for ammonia quantification by UV-colorimetric analysis using a commercial ammonia test kit. The ammonia calibration graphs were derived using known ammonia concentrations with a UV-vis spectrometer (Supplementary Figure S1). UV-vis spectra for the sampled electrolytes under various potentials were observed to display varied intensities indicating the concentration of ammonia. The ammonia concentration was calculated from the calibration graphs, and the ammonia yield rate and FE from Equation 2 and Equation 3, respectively. Figures 3B, C represent the CA curves and UV plots for Mo_2C-$Mo_2N_{0.92}$ electrocatalyst at various applied potentials, respectively. Similarly, the LSV curves for $Mo_2N_{0.92}$-Mo_2C electrocatalyst reveal a higher current density under N_2-saturation, indicating NRR (Figure 3D). Figures 3E, F represents the CA plots and corresponding UV curves for the prepared $Mo_2N_{0.92}$-Mo_2C electrocatalyst for ammonia quantification.

Figure 4A represents ammonia yield rates and FE of Mo_2C-$Mo_2N_{0.92}$ and $Mo_2N_{0.92}$-Mo_2C electrocatalysts for various applied potentials, respectively. A maximum ammonia yield of about 9.6 μg h^{-1} cm^{-2} and 6.61 μg h^{-1} cm^{-2} at −0.3 V vs. RHE was observed for Mo_2C-$Mo_2N_{0.92}$ and $Mo_2N_{0.92}$-Mo_2C electrocatalyst, respectively. Consequently, a maximum FE of about 10.15% and 4.21% at −0.1 V vs. RHE was observed for Mo_2C-$Mo_2N_{0.92}$ and $Mo_2N_{0.92}$-Mo_2C electrocatalyst, respectively. A comparatively high current density was observed under N_2 flow but a lower FE for ammonia of about 4.21% was observed at −0.1 V vs. RHE for $Mo_2N_{0.92}$-Mo_2C electrocatalyst. HER is kinetically favorable due to the comparatively low potential required for H_2 evolution than to dissociate the stable triple bonds of N_2. Thereby, the low FE for

ammonia can be attributed to the undesired HER with increasing negative potentials. Moreover, the particle sizes of Mo_2C-$Mo_2N_{0.92}$ and $Mo_2N_{0.92}$-Mo_2C from SEM images were observed to be 50 nm and 110 nm, respectively. It is suggested that a smaller size of the particles enables higher surface area and high exposure of active sites to drive the required electrochemical reactions. Consequently, Mo_2C-$Mo_2N_{0.92}$ electrocatalysts with a particle size of about 50 nm exhibits a higher NRR performance compared to $Mo_2N_{0.92}$-Mo_2C electrocatalysts with a higher particle size of about 110 nm. Therefore, particle sizes play an important role in determining the effective NRR performances for Mo_2C-$Mo_2N_{0.92}$ electrocatalysts.

Besides, a comparatively lower ammonia yield and FE was observed for $Mo_2N_{0.92}$-Mo_2C electrocatalyst, which can be due to the less activity of $Mo_2N_{0.92}$ phases for N_2 reduction. The NRR performances for bare Mo_2C and bare Ni foam were analyzed, which reveal a maximum ammonia yield of about 4.53 μg h^{-1} cm^{-2} and 0.07 μg h^{-1} cm^{-2} and FE of about 0.14% and 0.03%, respectively (Supplementary Figure S2). This poor NRR performance for bare Mo_2C and bare Ni foam substrate indicates the synergistic activity of the Mo_2C-$Mo_2N_{0.92}$ electrocatalyst. Figure 4B illustrates the NRR mechanism in the prepared Mo_2C-$Mo_2N_{0.92}$ heterostructures. The Mo_2C phases in the Mo_2C-$Mo_2N_{0.92}$ electrocatalyst generate ammonia by the electrochemical associative pathway by protonating the external N_2 gas and the Mo_2N phases following the MvK pathway by protonating the lattice-N to ammonia.

Mo_2C-$Mo_2N_{0.92}$ electrocatalyst has revealed considerably higher NRR performances due to the combined activity of the Mo_2C and $Mo_2N_{0.92}$ phases. N_2 adsorption and activation over an electrocatalyst surface occur at the exposed active sites. Previous studies have observed a strong N_2 adsorption behavior for Mo_2C,
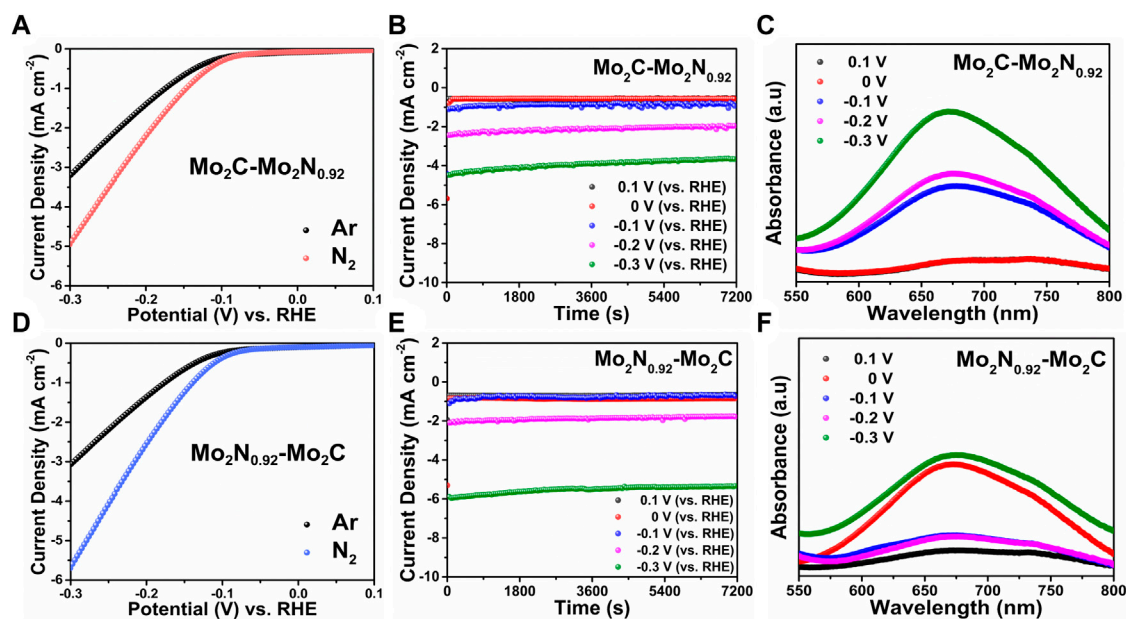
FIGURE 3
(A) LSV curves, (B) CA tests at various applied potentials, (C) UV-vis plots for corresponding CA test samples for Mo_2C-$Mo_2N_{0.92}$ electrocatalyst. (D) LSV curves, (E) CA tests at various applied potentials, and (F) UV-vis plots for corresponding CA test samples for $Mo_2N_{0.92}$-Mo_2C electrocatalyst.
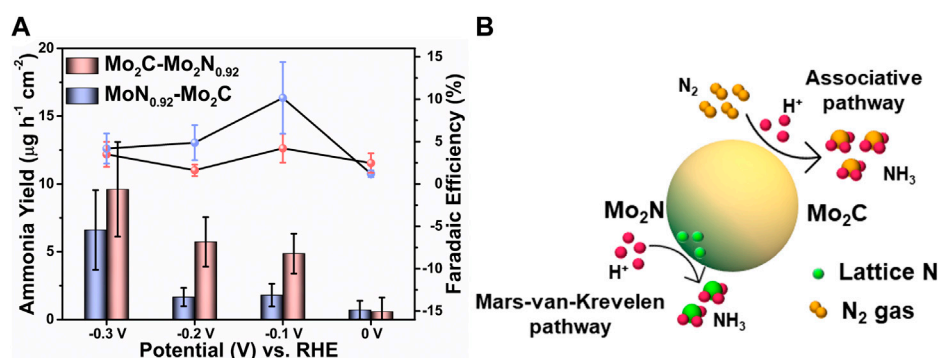
FIGURE 4
(A) Comparison of the ammonia yield and FE of Mo_2C-$Mo_2N_{0.92}$ and $Mo_2N_{0.92}$-Mo_2C electrocatalysts for various applied potentials. (Error bars indicate the range of values after three independent experiments) (B) Schematic illustration of NRR mechanism over Mo_2C-Mo_2N electrocatalyst.

which reveals a promising NRR electrocatalyst (Wan et al., 2022). Especially, the electron-rich Mo atoms with moderate H adsorption energy and high N_2 affinity are the main electrocatalytic active sites for NRR (Ma et al., 2020; Liu et al., 2021; Zhang et al., 2018a).

NRR takes place by the 'acceptance-donation' mechanism at the Mo active sites is explained as follows. The lone pair of electrons from the σ-orbitals of N_2 are donated into the empty d-orbitals of Mo, resembling acceptance, followed by the back-donation of the d-orbital electrons into the π* orbitals of N_2, resembling donation (Fan et al., 2022; Wan et al., 2022). This acceptance-donation mechanism over Mo active centers results in the activation of the highly stable triple bonds of N_2 and realizes an increase in bond length ((Mo)-N=N•), as shown in Equation 7. The chemisorbed N_2 on Mo active sites is further

protonated by six proton-coupled electron transfer steps (PCET) to form ammonia (Equation 8) by associative mechanism (Cheng et al., 2018; Ren et al., 2019).

$$\text{Activation step: } N_2 + (Mo) \rightarrow (Mo) - N = N\bullet \quad (7)$$

$$\text{Overall reaction: } (Mo) - N = N\bullet + 6\,H_2O + 6\,e^- \rightarrow 2\,NH_3 + 6\,OH^-$$
$$(8)$$
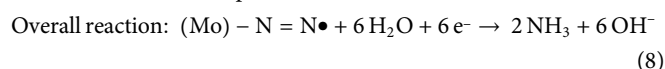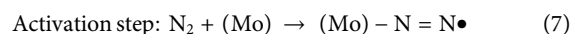
The associative mechanism for ammonia production over the Mo electrocatalytic active sites can be suggested as follows. Further, the activated N_2 can follow either an alternating protonating pathway or a distal protonating pathway.

$$(Mo) - N = N\bullet + H_2O + e^- \rightarrow (Mo) - N = NH + OH^- \quad (9)$$

Distal associative pathway

$$(Mo) - N = NH + H_2O + e^- \rightarrow (Mo) - N - NH_2 + OH^- \quad (10)$$

$$(Mo)-N-NH_2 + H_2O + e^- \rightarrow (Mo)-N-NH_3 + OH^- \rightarrow (Mo)-N + NH_3 \uparrow \quad (11)$$

$$(Mo) - N + H_2O + e^- \rightarrow (Mo) - NH + OH^- \quad (12)$$

$$(Mo) - NH + H_2O + e^- \rightarrow (Mo) - NH_2 + OH^- \quad (13)$$

$$(Mo) - NH_2 + H_2O + e^- \rightarrow (Mo) - NH_3 + OH^- \rightarrow (Mo) + NH_3 \uparrow \quad (14)$$
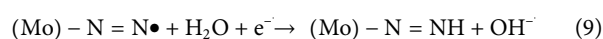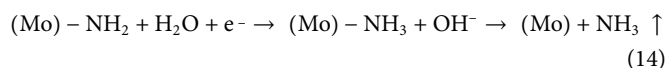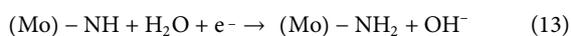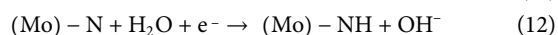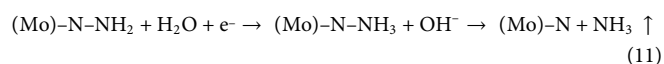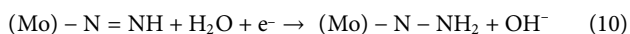
Alternating associative pathway

$$(Mo) - N = NH + H_2O + e^- \rightarrow (Mo) - NH - NH + OH^- \quad (15)$$

$$(Mo) - NH = NH + H_2O + e^- \rightarrow (Mo) - NH - NH_2 + OH^- \quad (16)$$

$$(Mo) - NH = NH_2 + H_2O + e^- \rightarrow (Mo) - NH_2 - NH_2 + OH^- \quad (17)$$

$$(Mo) - NH_2 - NH_2 + H_2O + e^- \rightarrow (Mo) - NH_2 - NH_3 + OH^- \rightarrow (Mo) - NH_2 + NH_3 \uparrow \quad (18)$$

$$(Mo) - NH_2 + H_2O + H_2O + e^- \rightarrow (Mo) - NH_3 \rightarrow (Mo) + NH_3 \uparrow \quad (19)$$
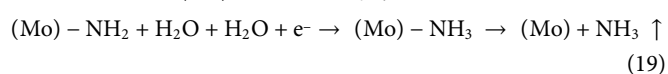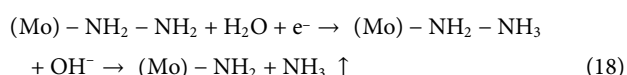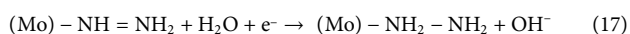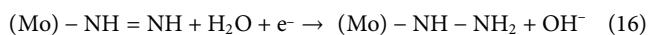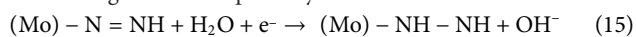
In the distal associative pathway, the protonation occurs from the farther side of the activated N atom (Equations 9-11). The protonation of the N atom bonded to the active site initiates only after complete protonation and ammonia evolution of the farthest N atom (Equations 12–14). In the alternating pathway, the protonation occurs alternatively on both N atoms and ammonia is generated at the final successive steps (Equations 15–19). Typically, the charge transfer reaction takes place *via* the charge accumulation and depletion stages in both Mo and N atoms attributing to better NRR performances (Wan et al., 2022).

Besides, $Mo_2N_{0.92}$ is suggested to generate ammonia by decomposition of the Mo_2N lattice rather than by catalytic mechanism (Zhang et al., 2018b; Hu et al., 2019). Thereby, the $Mo_2N_{0.92}$ entity present in the $Mo_2C-Mo_2N_{0.92}$ electrocatalyst generates ammonia by the Mars-van-Krevelen (MvK) mechanism. By the MvK mechanism, the lattice N atoms in metal nitride electrocatalysts are protonated rather than the conversion of gaseous N_2 to form ammonia (Equations 20–22) (Yang et al., 2019). The detailed MvK mechanism over Mo_2N phases is elucidated as follows.

$$Mo_2N + H_2O + e^- \rightarrow Mo_2(NH) + OH^- \quad (20)$$

$$Mo_2(NH) + H_2O + e^- \rightarrow Mo_2(NH_2) + OH^- \quad (21)$$

$$Mo_2(NH_2) + H_2O + e^- \rightarrow Mo_2(NH_3) + OH^- \rightarrow Mo_2^* + NH_3 \uparrow \quad (22)$$

$$Mo_2^* + N_2 \rightarrow Mo_2(N \equiv N) \ (Surface\ replenishment) \quad (23)$$

$$Mo_2(N \equiv N) + H_2O + e^- \rightarrow Mo_2(N \equiv NH_2) + OH^- \quad (24)$$

$$Mo_2(N = NH) + H_2O + e^- \rightarrow Mo_2(N - NH_2) + OH^- \quad (25)$$

$$Mo_2(N-NH_2) + H_2O + e^- \rightarrow Mo_2(N-NH_3) + OH^- \rightarrow Mo_2(N) + NH_3 \uparrow \quad (26)$$
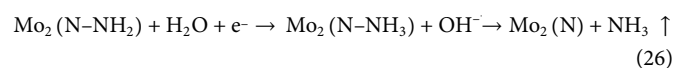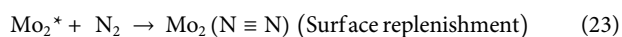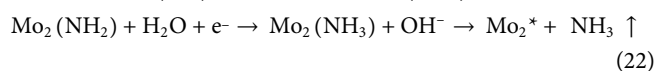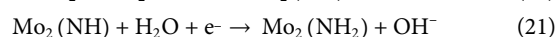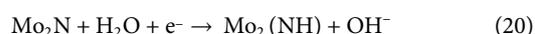
Where Mo_2^* represents the nitrogen vacancy formed due to the MvK mechanism. The surface replenishment of the nitrogen vacancies from N_2 occurs, which generates ammonia (Equation 23) (Abghoui et al., 2016). In cases due to low N_2 solubility in aqueous electrolytes, the surface nitrogen vacancies are replaced by the N atoms from the bulk resulting in the degradation of the electrocatalyst over time. Thereby, the surface replenished N is

then protonated to release ammonia (Equations 24–26). Besides, the MvK mechanism demands high energy for NRR, which facilitates HER at higher potentials (Ren et al., 2018). Nitrogen vacancies affect the neighboring N atoms in the lattice resulting in poor electrocatalytic performances (Ren et al., 2018). As a result, an increased ammonia yield due to the heterostructure formation can be ascribed to the combined contribution from electrochemical N_2 reduction and the MvK mechanism. The NRR performances in the prepared $Mo_2C-Mo_2N_{0.92}$ electrocatalysts reveal the combined activity of the Mo_2C and $Mo_2N_{0.92}$ phases. Hence, the combined electrochemical associative mechanism for N_2 reduction *via* Mo_2C and the MvK pathway by lattice-N protonation *via* $Mo_2N_{0.92}$ resulted in a high ammonia yield compared to the pristine counterparts.

3.3 Electrochemical characterization

Electrochemical impedance spectroscopy (EIS) analysis was undergone to elucidate the impedance characteristics of the prepared electrocatalysts. The Nyquist plots for real part (Z′) and imaginary part (Z″) of impedance elucidate the charge transfer and diffusion characteristics of the prepared electrocatalysts. The initial intercept on Z' axis at the high frequency region denotes the solution resistance (R_s) in the electrode and electrolyte interface. Besides, the diameter of the semi-circle in the mid-frequency region denotes the charge transfer resistance (R_{ct}) for the redox reactions between the active sites of the electrode and the electrolytic ions. Additionally, the linear curve in the low frequency region ascribes to the diffusion characteristics of the prepared electrocatalysts.

From the Nyquist plots in Figure 5A, $Mo_2C-Mo_2N_{0.92}$ electrocatalyst exhibits a low R_s value of about 11 Ω compared to $Mo_2N_{0.92}-Mo_2C$ (15 Ω) electrocatalyst. Besides, the $Mo_2C-Mo_2N_{0.92}$ electrocatalyst reveals R_{ct} value of about 4.5 Ω which is very less compared to 6.5 Ω for $Mo_2N_{0.92}-Mo_2C$ electrocatalyst. Thereby, the $Mo_2C-Mo_2N_{0.92}$ electrocatalyst is observed to exhibit faster electrocatalytic redox reactions superior to $Mo_2N_{0.92}-Mo_2C$ electrocatalyst. The superior electrocatalytic activity of the dominant Mo_2C phases in $Mo_2C-Mo_2N_{0.92}$ electrocatalyst explains the reduced resistance for redox reactions. Additionally, a higher angle for the linear curve with respect to *x*-axis was observed for $Mo_2C-Mo_2N_{0.92}$ in the low frequency region compared to $Mo_2N_{0.92}-Mo_2C$ which indicate the superior diffusion characteristics of the $Mo_2C-Mo_2N_{0.92}$ electrocatalyst.

The Nyquist admittance plots explain the conductivity of the prepared electrocatalysts as a function of frequency. The admittance plot is characterized by the knee frequency which elucidate the corresponding charge transfer resistances of the prepared electrocatalysts. From Figure 5B, the $Mo_2C-Mo_2N_{0.92}$ electrocatalyst displays a higher knee frequency at 58.52 Hz compared to $Mo_2N_{0.92}-Mo_2C$ (26.68 Hz). The higher knee frequency substantiates the lower charge transfer resistance for $Mo_2C-Mo_2N_{0.92}$ electrocatalyst which agrees with the Nyquist plots. The Bode phase plot in Figure 5C for the prepared electrocatalysts were obtained from the phase angle vs. frequency plots to elucidate the frequency response of the
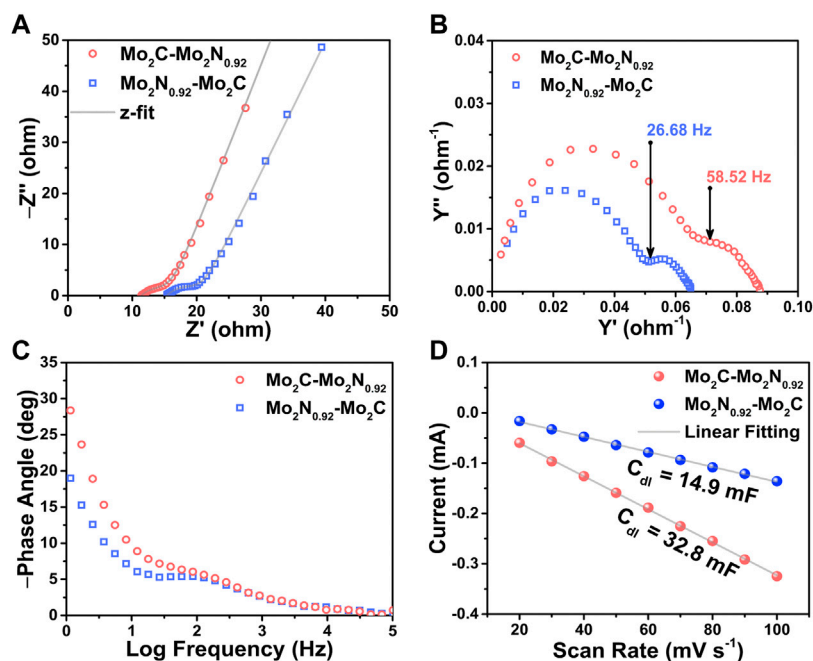
FIGURE 5
(A) Nyquist impedance plots, **(B)** Nyquist admittance plots, and **(C)** Bode plots for the prepared Mo_2C-$Mo_2N_{0.92}$ and $Mo_2N_{0.92}$-Mo_2C electrocatalysts, respectively. **(D)** Current vs. scan rate plots derived from CV curves performed at various scan rates.

electrocatalyst. The phase angle denotes the phase difference between the current and voltage of the electrochemical cell. A phase angle of $-90°$ denotes the ideal capacitor behavior elucidating a double-layer capacitance (C_{dl}). The curves in the low frequency region of the Bode phase plot denote the double layer capacitance(C_{dl}) of the electrocatalyst and the curves in high frequency region denote the capacitance in the redox reactions. Thereby, the Bode phase plots suggest a slight phase angle shift towards high frequencies for Mo_2C-$Mo_2N_{0.92}$ electrocatalyst than $Mo_2N_{0.92}$-Mo_2C indicating faster reaction kinetics. Hence, the dominant phases of Mo_2C in Mo_2C-$Mo_2N_{0.92}$ electrocatalyst drives a faster reaction kinetics than the $Mo_2N_{0.92}$ phases which validate the previous electrochemical studies.

Electrochemical active surface area (ECSA) of the prepared electrocatalysts were measured to estimate the available surface area for electrochemical reactions. ECSA was estimated by calculating the double layer capacitance (C_{dl}) of the prepared electrocatalysts by performing CV tests for various scan rates in the non-faradaic region, as shown in Figure 5D (Supplementary Figure S3). The current response in the non-faradaic region is purely due to the charge/discharge of the double layer. Thereby, the C_{dl} value (mF) was estimated from the slope of the linear plot of scan rate vs. current density derived from the CV curves. Consequently, the ratio of the C_{dl} value and the specific capacitance ($40 \mu F\, cm^{-2}$) yields ECSA value of the prepared electrocatalyst. As per the discussion, the electrocatalysts exhibit C_{dl} values of about 32.8 mF and 14.9 mF for Mo_2C-$Mo_2N_{0.92}$ and $Mo_2N_{0.92}$-Mo_2C, respectively. Consequently, the electrocatalysts exhibit a high ECSA value of about $820\, cm^2$ and $372.5\, cm^2$ for Mo_2C-$Mo_2N_{0.92}$ and $Mo_2N_{0.92}$-Mo_2C electrocatalyst, respectively.

Thereby, a high ECSA value attributes to higher exposure of active sites to the electrolytic ions for redox reactions.

4 Conclusion

In summary, the prepared Mo_2C-$Mo_2N_{0.92}$ electrocatalyst was synthesized by urea glass route under varying urea amounts followed by pyrolysis at $800°C$ under an N_2 atmosphere. The structural analysis reveals the formation of well-matched phases for Mo_2C-$Mo_2N_{0.92}$ samples respectively. The morphological and microstructure analysis reveals the formation of nanocomposites and well-defined lattice planes for Mo_2C-$Mo_2N_{0.92}$. The chemical state analysis of the prepared samples reveal the presence of metallic Mo bonds in addition to Mo_2N and Mo_2C. The electron-rich Mo sites act as the active sites for electrocatalytic NRR activity. NRR performances reveal a maximum ammonia yield of around $9.6 \mu g\, h^{-1}\, cm^{-2}$ at -0.3 V vs. RHE and an FE of about 10.15% at -0.1 V vs. RHE for Mo_2C-$Mo_2N_{0.95}$ electrocatalyst, respectively. The improved NRR performances were attributed to the synergistic activity of the Mo_2C and $Mo_2N_{0.92}$ moieties, which is verified by the NRR activity of the single-phase Mo_2C sample. Therefore, this study recommends the superior electrocatalytic activity of the tailored transition metal carbide and nitride electrocatalysts which could be further engineered to achieve efficient electrocatalysis.

Data availability statement

The raw data supporting the conclusions of this article will be made available by the authors, without undue reservation.

Author contributions

TA, SS, JK, and US contributed to conception and design of the study. TA and SS organized the database. TA performed the statistical analysis. TA and SS wrote the first draft of the manuscript. TA, SS, SJ, HL, DM, JK, and US wrote sections of the manuscript. All authors contributed to manuscript revision, read, and approved the submitted version.

Funding

Conflict of interest

The authors declare that the research was conducted in the absence of any commercial or financial relationships that could be construed as a potential conflict of interest.

Publisher's note

All claims expressed in this article are solely those of the authors and do not necessarily represent those of their affiliated organizations, or those of the publisher, the editors and the reviewers. Any product that may be evaluated in this article, or claim that may be made by its manufacturer, is not guaranteed or endorsed by the publisher.

Supplementary material

The Supplementary Material for this article can be found online at: https://www.frontiersin.org/articles/10.3389/fchem.2023.1122150/full#supplementary-material

References

Abghoui, Y., Garden, A. L., Howalt, J. G., Vegge, T., and Skúlason, E. (2016). Electroreduction of N2 to ammonia at ambient conditions on mononitrides of Zr, Nb, Cr, and V: A dft guide for experiments. *ACS Catal.* 6, 635–646. doi:10.1021/acscatal.5b01918

Arif, M., Babar, M., Azhar, U., Sagir, M., Bilal Tahir, M., Asim Mushtaq, M., et al. (2023). Rational design and modulation strategies of Mo-based electrocatalysts and photo/electrocatalysts towards nitrogen reduction to ammonia (NH3). *Chem. Eng. J.* 451, 138320. doi:10.1016/j.cej.2022.138320

Avery, W. H. (1988). A role for ammonia in the hydrogen economy. *Int. J. Hydrogen Energy* 13, 761–773. doi:10.1016/0360-3199(88)90037-7

Chen, S., Zhou, Z., Bai, B., Dai, Z., and Shi, J. (2022). *In-situ*-generated MoO2 on MoS2/ZnO heterostructures with enriched S,O-vacancies for enhanced electrocatalytic reduction of N2 to NH3. *ChemElectroChem* 9, e202200625. doi:10.1002/celc.202200625

Cheng, H., Ding, L.-X., Chen, G.-F., Zhang, L., Xue, J., and Wang, H. (2018). Molybdenum carbide nanodots enable efficient electrocatalytic nitrogen fixation under ambient conditions. *Adv. Mater.* 30, 1803694. doi:10.1002/adma.201803694

Chu, K., Li, X., Tian, Y., Li, Q., and Guo, Y. (2022). Boron nitride quantum dots/Ti3C2tx-MXene heterostructure for efficient electrocatalytic nitrogen fixation. *ENERGY and Environ. Mater.* 5, 1303–1309. doi:10.1002/eem2.12247

Cui, X., Tang, C., and Zhang, Q. (2018). A review of electrocatalytic reduction of dinitrogen to ammonia under ambient conditions. *Adv. Energy Mater.* 8, 1800369. doi:10.1002/aenm.201800369

Du, L., Xing, L., Zhang, G., Liu, X., Rawach, D., and Sun, S. (2021). Engineering of electrocatalyst/electrolyte interface for ambient ammonia synthesis. *SusMat* 1, 150–173. doi:10.1002/sus2.7

Fan, B., Wang, H., Zhang, H., Song, Y., Zheng, X., Li, C., et al. (2022). Phase transfer of Mo2C induced by boron doping to boost nitrogen reduction reaction catalytic activity. *Adv. Funct. Mater.* 32, 2110783. doi:10.1002/adfm.202110783

Fiksel, J., Bruins, R., Gatchett, A., Gilliland, A., and ten Brink, M. (2014). The triple value model: A systems approach to sustainable solutions. *Clean Technol. Environ. Policy* 16, 691–702.

Giordano, C., Erpen, C., Yao, W., and Antonietti, M. (2008). Synthesis of Mo and W carbide and nitride nanoparticles via a simple "urea glass" route. *Nano Lett.* 8, 4659–4663. doi:10.1021/nl8018593

Guo, X., Wan, X., and Shui, J. (2021). Molybdenum-based materials for electrocatalytic nitrogen reduction reaction. *Cell Rep. Phys. Sci.* 2, 100447. doi:10.1016/j.xcrp.2021.100447

Hargreaves, J. S. J. (2013). Heterogeneous catalysis with metal nitrides. *Coord. Chem. Rev.* 257, 2015–2031. doi:10.1016/j.ccr.2012.10.005

Hinnemann, B., and Nørskov, J. K. (2006). Catalysis by enzymes: The biological ammonia synthesis. *Top. Catal.* 37, 55–70. doi:10.1007/s11244-006-0002-0

Hu, B., Hu, M., Seefeldt, L., and Liu, T. L. (2019). Electrochemical dinitrogen reduction to ammonia by Mo2N: Catalysis or decomposition? *ACS Energy Lett.* 4, 1053–1054. doi:10.1021/acsenergylett.9b00648

Huo, L., Liu, B., Zhang, G., and Zhang, J. (2016). Universal strategy to fabricate a two-dimensional layered mesoporous Mo2C electrocatalyst hybridized on graphene sheets with high activity and durability for hydrogen generation. *ACS Appl. Mater. Interfaces* 8, 18107–18118. doi:10.1021/acsami.6b05007

Kandemir, T., Schuster, M. E., Senyshyn, A., Behrens, M., and Schlögl, R. (2013). The haber–bosch process revisited: On the real structure and stability of "ammonia iron" under working conditions. *Angew. Chem. Int. Ed.* 52, 12723–12726. doi:10.1002/anie.201305812

Liu, J., Kong, W., Jin, Z., Han, Y., Sun, J., Ma, L., et al. (2020). A MoFe nitrogenase-mimicking electrocatalyst for nitrogen fixation with high faradaic efficiency. *J. Mater. Chem. A* 8, 19278–19282. doi:10.1039/d0ta07757g

Liu, W., Wang, X., Wang, F., Du, K., Zhang, Z., Guo, Y., et al. (2021). A durable and pH-universal self-standing MoC–Mo2C heterojunction electrode for efficient hydrogen evolution reaction. *Nat. Commun.* 12, 6776. doi:10.1038/s41467-021-27118-6

Ma, Y., Yang, T., Zou, H., Zang, W., Kou, Z., Mao, L., et al. (2020). Synergizing Mo single atoms and Mo2C nanoparticles on CNTs synchronizes selectivity and activity of electrocatalytic N2 reduction to ammonia. *Adv. Mater.* 32, 2002177. doi:10.1002/adma.202002177

MacFarlane, D. R., Cherepanov, P. V., Choi, J., Suryanto, B. H. R., Hodgetts, R. Y., Bakker, J. M., et al. (2020). A roadmap to the ammonia economy. *Joule* 4, 1186–1205. doi:10.1016/j.joule.2020.04.004

Mtukula, A. C., Bo, X., and Guo, L. (2017). Highly active non-precious metal electrocatalyst for the hydrogen evolution reaction based on nitrogen-doped graphene supported MoO2/WN/Mo2N. *J. Alloys Compd.* 692, 614–621. doi:10.1016/j.jallcom.2016.09.079

Ren, X., Cui, G., Chen, L., Xie, F., Wei, Q., Tian, Z., et al. (2018). Electrochemical N2 fixation to NH3 under ambient conditions: Mo2N

nanorod as a highly efficient and selective catalyst. *Chem. Commun.* 54, 8474–8477. doi:10.1039/c8cc03627f

Ren, X., Zhao, J., Wei, Q., Ma, Y., Guo, H., Liu, Q., et al. (2019). High-performance N2-to-NH3 conversion electrocatalyzed by Mo2C nanorod. *ACS Central Sci.* 5, 116–121. doi:10.1021/acscentsci.8b00734

Ren, Y., Yu, C., Tan, X., Huang, H., Wei, Q., and Qiu, J. (2021). Strategies to suppress hydrogen evolution for highly selective electrocatalytic nitrogen reduction: Challenges and perspectives. *Energy and Environ. Sci.* 14, 1176–1193. doi:10.1039/d0ee03596c

Safari, A., Das, N., Langhelle, O., Roy, J., and Assadi, M. (2019). Natural gas: A transition fuel for sustainable energy system transformation? *Energy Sci. Eng.* 7, 1075–1094. doi:10.1002/ese3.380

Sardar, K., Dan, M., Schwenzer, B., and Rao, C. N. R. (2005). A simple single-source precursor route to the nanostructures of AlN, GaN and InN. *J. Mater. Chem.* 15, 2175–2177. doi:10.1039/b502887f

Su, D., Zhang, X., Wu, A., Yan, H., Liu, Z., Wang, L., et al. (2019). CoO-Mo2N hollow heterostructure for high-efficiency electrocatalytic hydrogen evolution reaction. *NPG Asia Mater.* 11, 78. doi:10.1038/s41427-019-0177-z

Wan, Y., Wang, Z., Li, J., and Lv, R. (2022). Mo2C-MoO2 heterostructure quantum dots for enhanced electrocatalytic nitrogen reduction to ammonia. *ACS Nano* 16, 643–654. doi:10.1021/acsnano.1c07973

Wang, T., Wang, P., Zang, W., Li, X., Chen, D., Kou, Z., et al. (2022). Nanoframes of Co3O4–Mo2N heterointerfaces enable high-performance bifunctionality toward both electrocatalytic HER and OER. *Adv. Funct. Mater.* 32, 2107381. doi:10.1002/adfm.202107382

Yang, X., Kattel, S., Nash, J., Chang, X., Lee, J. H., Yan, Y., et al. (2019). Quantification of active sites and elucidation of the reaction mechanism of the electrochemical nitrogen reduction reaction on vanadium nitride. *Angew. Chem. Int. Ed.* 58, 13906–13910. doi:10.1002/ange.201906449

Ye, T., Ba, K., Yang, X., Xiao, T., Sun, Y., Liu, H., et al. (2023). Valence engineering at the interface of MoS2/Mo2C heterostructure for bionic nitrogen reduction. *Chem. Eng. J.* 452, 139515. doi:10.1016/j.cej.2022.139515

Yesudoss, D. K., Lee, G., and Shanmugam, S. (2021). Strong catalyst support interactions in defect-rich γ-Mo2N nanoparticles loaded 2D-h-BN hybrid for highly selective nitrogen reduction reaction. *Appl. Catal. B Environ.* 287, 119952. doi:10.1016/j.apcatb.2021.119952

Yuan, S., Xia, M., Liu, Z., Wang, K., Xiang, L., Huang, G., et al. (2022). Dual synergistic effects between Co and Mo2C in Co/Mo2C heterostructure for electrocatalytic overall water splitting. *Chem. Eng. J.* 430, 132697. doi:10.1016/j.cej.2021.132697

Yue, M., Lambert, H., Pahon, E., Roche, R., Jemei, S., and Hissel, D. (2021). Hydrogen energy systems: A critical review of technologies, applications, trends and challenges. *Renew. Sustain. Energy Rev.* 146, 111180. doi:10.1016/j.rser.2021.111180

Zhang, L., Ji, X., Ren, X., Luo, Y., Shi, X., Asiri, A. M., et al. (2018). Efficient electrochemical N2 reduction to NH3 on Mon nanosheets array under ambient conditions. *ACS Sustain. Chem. Eng.* 6, 9550–9554. doi:10.1021/acssuschemeng.8b01438

Zhang, L., Ji, X., Ren, X., Ma, Y., Shi, X., Tian, Z., et al. (2018). Electrochemical ammonia synthesis via nitrogen reduction reaction on a MoS2 catalyst: Theoretical and experimental studies. *Adv. Mater.* 30, 1800191. doi:10.1002/adma.201800191

Zhang, Y., Guo, P., Guo, S., Xin, X., Wang, Y., Huang, W., et al. (2022). Gradient heating epitaxial growth gives well lattice-matched Mo2C–Mo2N heterointerfaces that boost both electrocatalytic hydrogen evolution and water vapor splitting. *Angew. Chem. Int. Ed.* 61, e202209703. doi:10.1002/anie.202209703

Zhao, Y., Setzler, B. P., Wang, J., Nash, J., Wang, T., Xu, B., et al. (2019). An efficient direct ammonia fuel cell for affordable carbon-neutral transportation. *Joule* 3, 2472–2484. doi:10.1016/j.joule.2019.07.005

Zhou, L. (2005). Progress and problems in hydrogen storage methods. *Renew. Sustain. Energy Rev.* 9, 395–408. doi:10.1016/j.rser.2004.05.005